International Journal of Heat and Mass Transfer 194 (2022) 123003

Contents lists available at ScienceDirect

International Journal of Heat and Mass Transfer

journal homepage: www.elsevier.com/locate/hmt

Atomistic evidence of hydrodynamic heat transfer in nanowires

Paul Desmarchelier[a,*], Albert Beardo[b], F. Xavier Alvarez[b], Anne Tanguy[c,d], Konstantinos Termentzidis[a]

[a] Univ Lyon, CNRS, INSA Lyon, CETHIL, UMR5008, Villeurbanne, 69621, France
[b] Physics Department, Universitat Autónoma de Barcelona, Catalonia, 08193, Spain
[c] Univ Lyon, INSA Lyon, CNRS, LaMCoS, UMR5259, Villeurbanne, 69621, France
[d] ONERA, University Paris-Saclay, Chemin de la Huniére, BP 80100, Palaiseau, 92123, France

ARTICLE INFO

Article history:
Received 9 February 2022
Revised 13 April 2022
Accepted 5 May 2022

Keywords:
Hydrodynamic heat transport
Nanowires
Amorphous shell
Nanocomposites

ABSTRACT

With wave-packet propagation simulations and heat flux estimation via molecular dynamics, we show that the heat flux radial distribution in silicon nanowires can be described by a mesoscopic model, the hydrodynamic heat equation. We observe Poiseuille like heat flux profile, that cannot be described by a simple kinetic model such as the Fuchs-Sondheimer model, in both pristine and core/shell nanowires. The addition of a shell does not change the shape of the radial heat flux distribution, but just modifies the maximum of the heat flux in the center of the nanowire. These results show that there is a heat flux depletion length for pristine or core shell nanowires, 1–2 nm away from the boundary of the crystalline part. The parameters of the mesoscopic model are discussed in terms of microscopic properties, including the phonon mean free path as function of frequency and the partial vibrational density of states in the different regions of the nanowire.

© 2022 Elsevier Ltd. All rights reserved.

1. introduction

Heat transfer at the nanoscale has been originally described using the linearized Peierls Boltzmann (PB) equation [1]. Among the pioneering models, the early kinetic theory models [2], or the Maxwell-Catteneo model [3] can be mentioned. They overcome some of the shortcomings of the conventional Fourier's law at the nanoscale, by modeling thermal transport in terms of the heat carrier dynamics and of interactions among themselves and with the lattice defects. Since then, numerous models of thermal transport at the nanoscale have been developed. These approaches can be separated into two main categories: those based on a continuum approach such as the Callaway Model [4] or Monte Carlo approaches [5], and those based on discrete representations such as Lattice Dynamics [6] or Atomic Green Functions [7].

Among the continuous medium solutions, a method of interest is the kinetic collective model [8]. It relies on a solution of the linearized PB equation, to derive the hydrodynamic heat equation [9]. This mesoscopic transport equation generalizes Fourier's law by including a non-local and a memory term, and it reduces to the diffusive description for large length and time scales. The original derivation was proposed to describe small size and high frequency effects in some specific materials at low temperatures, where momentum preserving phonon-phonon collisions dominate [10]. However, it has recently been shown that this description is also relevant for room temperature applications in general semiconductors like Si [9,11]. The derived set of equations can be solved using the finite element method, to model the thermal relaxation of nanostructured heat sources on Si substrate [12] or thermoreflectance experiments [13].

However, as the size of the object decreases, the continuous modeling reaches its limits, and the atomic structure of the material has to be explicitly accounted for. This is possible with Molecular Dynamics (MD). In MD, the trajectories and interaction forces of the atoms are explicitly computed. The temperature is defined via the kinetic energy fluctuation, and the heat flux via the interactions and movement of the particles [14]. This allows the computation of the thermal conductivity via the fluctuation dissipation theorem in the linear response approximation [15], or more simply by sustaining a thermal gradient and computing the resulting flux [16]. Alternatively, the thermal transfer can also be estimated using wave-packet (WP) simulations [17]. MD has the advantage that it does not rely on the phonon gas model, and the whole phonon spectrum is taken into account. However, as the electronic interactions are not explicitly considered, it has to rely on an approximated interaction potential. Moreover, as it is a fully classical method, its results are only valid above the Debye temperature.

* Corresponding author.
E-mail address: paul.desmarchelier@insa-lyon.fr (P. Desmarchelier).

https://doi.org/10.1016/j.ijheatmasstransfer.2022.123003
0017-9310/© 2022 Elsevier Ltd. All rights reserved.

Nevertheless, in this temperature range, this method is able to predict correctly the thermal properties of bulk Si [18].

These thermal transfer models are particularly useful to predict the thermal properties of the nano-objects developed and increasingly used during the last half century [19]. Silicon nanowires (NWs) are a good example. They were first discovered in the 60s, and have been used for many applications in the last twenty years [20]. They are a perfect example of small-scale devices for which the thermal conductivity depends on the size [21]. The reduction of thermal conductivity in these structures is often linked to non-local effects and phonon-boundary scattering [22], even though the phonon boundary scattering alone is not sufficient to explain the decrease in thermal conductivity [23]. In particular, the thermal conductivity is linked to surface roughness [24,25]. Interestingly, thermal properties can be tuned by the structuration of the NW, as it has been shown experimentally by etching [26] or via simulations with faceting [27]. A decrease of the thermal conductivity can be obtained, either by inducing back-scattering or by promoting diffusive scattering over reflection [24]. It has also been shown that phonon coherent effects due to the addition of a crystalline shell can also contribute to the reduction of thermal conductivity [28]. This influence of the boundaries leads to a non-uniform radial flux distribution, that can be observed in MD or in Monte-Carlo solvers of the PB equation [29,30].

However, Si NWs are rarely pristine. When exposed to oxygen, an amorphous oxide layer forms [31], and as phonon transmission at an amorphous/crystalline interface is possible [32], this may affect the phonon transport in the NW. Moreover, it has been shown that this interface influences the vibrational properties of the crystal near the interface [33]. Likewise, the interface decreases the ballistic heat transport in the NW [34]. The presence of the shell affects the heat transfer in the core, which can be seen as an effect of the interface parallel to the heat flux. Thus, the amorphous shell has to be considered for the estimation of the thermal properties of the crystalline core. Previous studies have already shown the effect of the amorphous shell structuration. For instance, a structural or geometric modulation of the shell can reduce the thermal conductivity [35,36] or induce rectification [37].

However, the impact of the amorphous layer on the distribution of flux was less studied. The work of Bejenari et al. on the radial temperature profile in NWs [38] and of Verdier et al. on the impact of the amorphization at constant crystalline layer thickness [39] can nevertheless be noted.

In this work, the radial flux distribution in pristine and core/shell Si NWs is obtained with MD and then analyzed at the mesoscopic level of description using the hydrodynamic heat transport equation. Such comparative studies between phonon hydrodynamic transport and MD have already been carried in telescopic Si NW [30], and used to model second sound in germanium [40]. First, the methods used and the NWs studied will be presented. Then, the radial flux distribution obtained with a wave packet method will be presented. Finally, the steady-state flux distribution obtained in non equilibrium molecular dynamics (NEMD) simulations is analyzed using the hydrodynamic heat equation.

2. methods

2.1. modeling core/shell nanowires

The configurations used here are silicon NWs, with a crystalline core radius R_{Cry} of 37.5 or 50 Å, and an eventual amorphous shell of thickness e from 10 to 20 Å (see Fig. 1). Their length is equal to 50 nm. The different dimensions, along with crystalline fraction ratio and the radial discretization parameter dr used for heat flux computation, are listed in Table 1. To create the core-shell nanowires, the external cylindrical shell is first cut out of an a-Si bulk block, that will be the amorphous shell surrounding the NW (in blue in Fig. 1). Then this hollow cylinder is filled with c-Si with the ⟨100⟩ direction of the crystal lattice in the principal direction of the NW. To simulate an infinite NW, periodic boundary conditions are used in the longitudinal direction and fixed ones in the other directions. The a-Si sample used was created in an earlier work [17]. The original sample is a cube of side 17.5 nm repeated three times to reach the appropriate length.

Table 1
Dimensions of the different configurations with R_{Cry} the crystalline radius, e the amorphous shell thickness, dr the radial resolution of the flux and N_c/N_t the crystalline fraction ratio.

R_{Cry} (Å)	37.5			50		
e (Å)	0	10	20	0	10	20
dr (Å)	2.5	2.5	2.5	2.5	5	5
N_c/N_t (%)	100	62	43	100	69	51

These nanowires are then relaxed with, first a conjugated gradient energy minimization to reach a local mechanical equilibrium, then an equilibration at 100 K with an isothermal/isobaric simulation for 10ps, followed by an isothermal equilibration at the same temperature for 10 ps. A time step of 1×10^{-3} ps is used for the equilibrations. After this annealing, a second conjugated gradient energy minimization is performed. We used a modified SW interatomic potential allowing a more realistic modeling of the interface between c-Si and a-Si in terms of interfacial energy and regular atomic energies inside the two phases [33].

2.2. kinetic collective model

The hydrodynamic heat equation relies on a solution of the linearized Peierls Boltzmann equation in a continuous medium to describe heat transport at the microscale [9]. The derivation is based on assuming that, for moderate Knudsen numbers, the perturbed phonon distribution function is an expansion in terms of the heat flux and its first derivatives in time and space. The solution is obtained for general linearized collision operators and general dispersion relations. Accordingly, the governing equation for the heat flux $\mathbf{j}$ and the temperature T in a crystalline medium is the following:

$$\mathbf{j} + \kappa_{Hyd}\nabla T + \tau \frac{\partial \mathbf{j}}{\partial t} = \ell^2[\nabla^2 \mathbf{j} + \alpha \nabla(\nabla \cdot \mathbf{j})], \tag{1}$$

with κ_{Hyd} the thermal conductivity, τ the heat flux relaxation time, ℓ the non-local length, α a coefficient [9]. The first two terms of Eq. (1) correspond to the usual Fourier's law. The last term in the left-hand side introduces the thermal inertial effect, appearing when the timescale is close to the phonon lifetime. The terms in the right-hand side introduce non-local effects that appear when the size of the system is of the order of the mean free path. This last term is analogous to the viscous term in Navier-Stokes equations describing fluid motion. For this reason, Eq. (1) is called the phonon hydrodynamic equation. If the original derivation was made for low-temperature applications for specific materials like graphene [10,41], it has been shown that it can be generalized for other materials at room temperature [11,12]. It is worth mentioning that, in the amorphous shell of the NWs, due to the reduced phonon lifetime, memory and nonlocal effects have been neglected, so the diffusive transport equation (2) is used instead of equation (1):

$$\mathbf{j} + \kappa \nabla T = 0. \tag{2}$$

To predict the thermal response of the system, the transport equation is combined with the energy conservation equation,

$$\nabla \cdot \mathbf{j} = -c_v \frac{\partial T}{\partial t}, \tag{3}$$

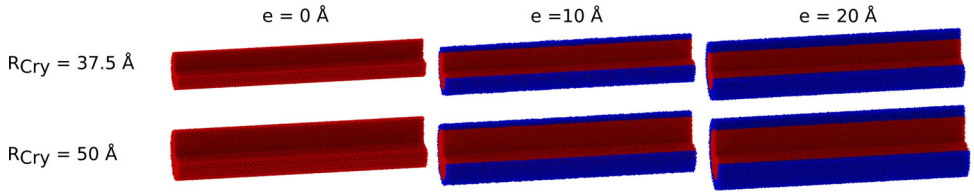


Fig. 1. Cross-sectional representation of the different configurations studied, with amorphous atoms in blue and the crystalline atoms in red. (For interpretation of the references to colour in this figure legend, the reader is referred to the web version of this article.)

with c_v the specific heat. Moreover, appropriate boundary conditions are required. For instance, in the present study, the continuity of the normal heat flux between the crystalline NW and the amorphous shell is imposed. Furthermore, the tangential heat flux $\mathbf{j_t}$ in the crystalline side of the interface is defined by the slip boundary condition:

$$\mathbf{j_t} = -C\ell\nabla\mathbf{j_t}\cdot\mathbf{n}, \tag{4}$$

with $\mathbf{n}$ the normal-boundary vector pointing towards the amorphous region, and C the slip coefficient weighting the amount of specular and diffusive phonon-boundary reflections [42]. Finally, in the free surfaces of the amorphous shell or the pristine NW, heat flux insulation ($\mathbf{j}\cdot\mathbf{n} = 0$) is imposed.

It is also worth to note that the applicability of the hydrodynamic heat transport model derived in [9] is limited to small enough Knudsen numbers. In the present work, the use of the *ab initio* calculated volumic parameters ℓ and κ_{Hyd} is precluded due to the small NW diameters [42]. However, the model can be still used with effective parameters to interpret the MD simulations as done for previous studies [30].

2.3. heat flux in molecular dynamics

The goal of this work, is to provide insights about the heat flux radial distribution in core/shell NWs, by comparing with the mesoscopic modeling based on Eq. (1). This requires the definition of the flux in MD. The heat flux in a volume V can be defined as [14]:

$$J = \frac{1}{V}\left(\sum_i^N E_i\mathbf{v_i} + \bar{\bar{\sigma}}_i\cdot\mathbf{v_i}\right), \tag{5}$$

with E_i the total energy of the atom i, $\mathbf{v_i}$ the velocity of atom i, $\frac{N}{V}\bar{\bar{\sigma}}_i$ the stress on atom i and N the number of atoms in the volume. The sum runs on every atom within the volume considered. The virial contribution (part due to the interaction with other particles, as opposed to the energy of the atom itself) $\bar{\bar{\sigma}}_i$ is computed as follows:

$$\bar{\bar{\sigma}}_i = -\sum_{k\in K_i}\frac{1}{N_k}\sum_{j\in k}\mathbf{r_j^k}\otimes\mathbf{F_j^k}, \tag{6}$$

with K_i the number of interaction involving the atom i, N_k the number of atom involved in the interaction, $\mathbf{r_j^k}$ the position of the atoms j, $\mathbf{F_j^k}$ the force acting on atom i due to the interaction with atom j for the k body interaction. This implementation is not exact for many body interaction potentials and correction have been proposed recently [43]. Nevertheless, for silicon the correction does not impact the results in terms of heat flux [44].

3. results

3.1. ballisticity as a function of the frequency

To identify the different energy pathways of the different monochromatic phonons, we have studied the propagation of wave-packets in the nanowires of R_{Cry}= 37.5 Å and $e = 0$ or 10 Å. These wave-packets are created through the excitation of central layer with a gaussian windowed sinusoidal excitation (see A.1). The selection of the NWs for this section is motivated by the economy of data, the largest NWs producing larger files.

The distribution of kinetic energy in a cross-section of the NWs at 2 and 12 THz are depicted in Fig. 2. At low frequencies, in the first two columns with or without shell, respectively, the wave-packets initially keep their plane wave shape, but are quickly dispersed. The WPs travel at different speeds in the different concentric regions of the NWs. This gives rise to interactions between the wave in the shell and the wave in the core, as discussed in a previous publication [37].

Moreover, at low frequencies, wave propagation is partly supported by the surfaces. This appears in Fig. 2, but also in Fig. 3 that shows that if we consider a portion of the NW (here a 70 Å thick slice 90 Å away from the excited layer) the energy at the free surface does not stay constant but increases with time. This indicates that energy travels at the free surface. It also appears that more energy travels at the surface in the presence of an amorphous shell. Moreover, this figure shows that without shell, a second energy peak appears at R = 20 Å. This is a consequence of the patterns appearing in the cross-sections.

At 12 THz, the energy propagates differently: it mainly flows in the core of the crystalline region. The profile of the propagating part of the WP is similar with or without shell, as depicted in the bottom panels of Fig. 3. Little to no energy propagates near the interface/surface, and even less in the amorphous shell. The energy concentration is maximum in the center of the NW and decreases when going toward the surface. This shape indicates a strong effect of the free surface or crystalline/amorphous interface on the energy propagation. At high frequencies, the main effect of the amorphous shell is the emergence of diffusive transport. This diffusive transport appears as a slowly expending red patch in the left part of the image in the fourth column of Fig. 2. This diffusive behavior was originally expected in the amorphous shell [45], more surprisingly, it also appears in the crystalline core when looking at the wave-packet propagation [37].

A more systematic study of the different frequencies shows that, most of the energy is carried by the center of the crystalline core away from the crystalline/amorphous interface or free surface (see A.1 for more details).

Overall, apart from the complex patterns that appear at 2 THz, the radial distribution of energy during WP propagation is not strongly impacted by the presence of the shell. This short study of the system through WP propagation, shows that even if the free surface seems to transport energy at low frequencies, most of it is transported by the inner part of the NWs away from the interface or free surface. However, the realistic reconstruction of the radial flux distribution from these simulations is not trivial. To access it more easily, NEMD simulations are performed.

3.2. heat flux radial distribution: Effect of the shell

To obtain the heat flux as a function of the radius, NEMD simulations are performed, with a thermal gradient of 40 K around 300 K across the NWs (see A.2). The results, in terms of ther-

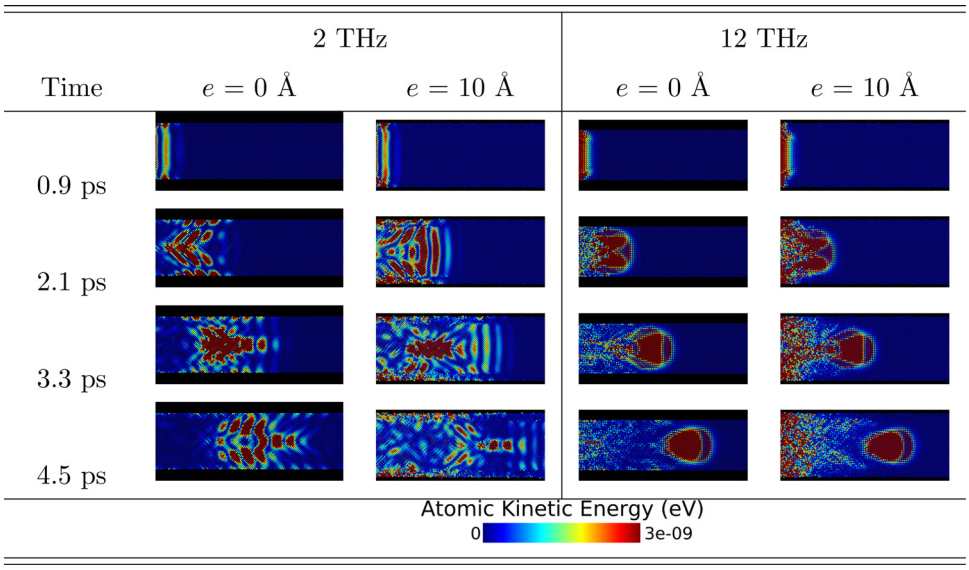


Fig. 2. Cross-sectional view of a wave-packet going through the nanowires of R_{Cry}= 37.5 Å and $e = 0$ or 10 Å. Only the right side of the NW is represented, the propagation on the left side being symmetric. The color scale in the bottom row going from 0 (blue) to 1×10^{-9}eV (dark red) gives the atomic kinetic energy. Between each line 1.2 ps has elapsed. (For interpretation of the references to colour in this figure legend, the reader is referred to the web version of this article.)

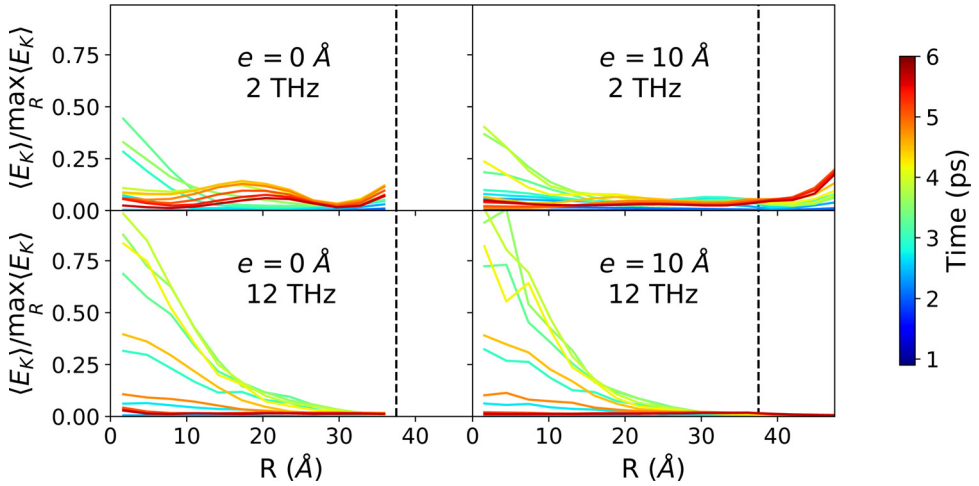


Fig. 3. Atomic kinetic energy as a function of the radius averaged on a portion of the NWs 90 to 160 Å away from the excited layer, for different time steps (colors). For the nanowires of R_{Cry} = 37.5 Å and $e = 0$ Å (first column) or $e = 10$ Å (second column) at 2 THz (first line) and 12 THz (second line). The values are normed by the maximum reached at 12 THz. The vertical black dashed line represents the end of the crystalline core.

mal flux radial distribution, for the nanowires of R_{Cry} = 37.5 Å are reported in Fig. 4. First, it appears that with or without shell the flux is maximum in the center of the NW, stays constant for R <20 Å and then decreases closer to the free surface/interface. This Poiseuille-like heat flux profile is very similar to what was observed by Verdier et al. [29]. In the amorphous shell (browned region), the heat flux does not depend on the radius and is constant at 1.2×10^9 W/m^2. There, the reduced phonon lifetime, renders the non-local effects negligible and diffusive transport (Eq. (2)) is fully recovered. The heat flux profile with or without shell are very similar, the only notable difference is the decrease of the flux in the center of the core in the presence of a shell. An overall reduction of the flux/thermal conductivity in the crystal due to the addition of an amorphous layer has already been observed for thin films [39].

We tried to explain the observed profile by changes of the vibrational properties of the NWs due to the free surface or the presence of the amorphous shell. A first explanation for the heat flux depletion near the surface/interface, can be looked for in the available vibrational modes. For instance, high frequency localized modes could appear in the region where the flux is decreased. Alternatively, a softening could be observed, explaining a local thermal conductivity decrease. To test this hypothesis, the partial vibrational density of states VDOS (see A.3) in the different layers of the NWs with or without shell are represented in the Fig. 5. It appears that only the crystalline layer within 5 Å of the surface/interface (red region) is affected. This corresponds to the layer where the structure of the crystal differs the most from bulk c-Si due to the surface/interface re-structuration or influence of the amorphous shell. In the inner core, the partial VDOS is very close to the one of c-Si, and in the amorphous shell very close to the one of a-Si. In the end, the perturbations of the partial VDOS does not extend to the whole region where the flux is reduced (the red region in Fig. 4 does not extend to the dashed line). As a result, the local flux variations cannot be explained simply by the local modification of the available modes in the NW core.

The radial heat flux profiles can be obtained using the hydrodynamic heat transport model. As explained in Section 2.2, the hydrodynamic heat transport equation is a continuous equation de-

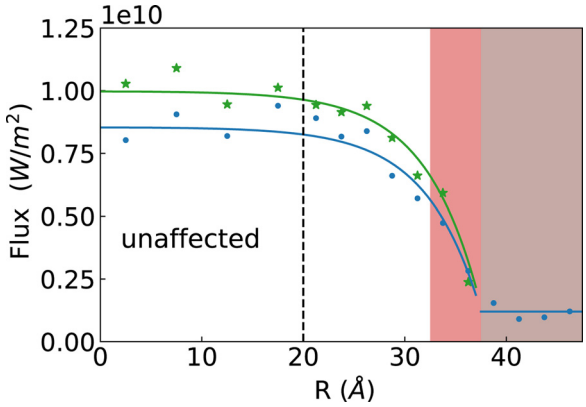


Fig. 4. Heat flux in the NW as a function of the radius for R_{Cry} = 37.5 Å and e = 0 (green) or 10 Å (blue). The dots or stars report the values obtained through the NEMD simulations in the different layers, and the full lines the flux obtained with the hydrodynamic heat transport model (Eqs. (1), (2) and (4)). The dotted line delimits where the shape of the flux distribution is influenced by the boundary (curved profile), and where it is not (flat profile). The brown region delimits the amorphous shell, and the red region shows the crystalline layer where the VDOS is affected due to the presence of the boundary (see Fig. 5). (For interpretation of the references to colour in this figure legend, the reader is referred to the web version of this article.)

rived from the Boltzmann transport equation. It adds the influence of memory and non-local effects to the usual diffusive transport mechanism [9]. Here, to reproduce the heat flux profile via the hydrodynamic equations, the same temperature gradient as for the MD simulation is imposed across the NW, and the different parameters of the Eqs. (1) and (4) are fitted to reproduce the results of NEMD simulations. This is done using the finite element method, with the software *COMSOL Multiphysics* [42]. Note that, as the steady state is considered reached, the conservation equation (3) is simplified to $\nabla \cdot \boldsymbol{j} = 0$, and the memory term in the transport Eq. (1) vanishes ($\frac{d\mathbf{j}}{dt} = 0$). Consequently, the only non-Fourier term that survives is the Laplacian term associated to shear viscosity effects $\ell^2[\nabla^2\mathbf{j}]$. To obtain systematic fits, each parameter is adjusted using different observables obtained in the MD simulations. The thermal conductivity κ_{Hyd} is set first to fit the amount of flux flowing in the central region, where the profile is flat and the viscous effects arising from the boundaries are unnoticeable. The non-local length ℓ is set to fit the size of the region where the flux profile is curved (i.e. the heat flux boundary layer size [42]). Finally, the slip coefficient C is fitted to reproduce the amount of flux flowing at the interface. The solid lines in Fig. 4, are obtained using this method, for the flux in the crystalline core. In the amorphous shell, the flux does not depend on the radius and is modeled by

Table 2
Values of the parameters of Eq. (1) and (4) used to obtain the heat flux profile of the different NWs.

R_{Cry} (Å)	e (Å)	κ_{Hyd} (W m^{-1}K$^{-1-1\ -1}$)	ℓ (Å)	C	κ_{shell} (W m^{-1}K^{-1})
37.5	0	12.5	5	0.3	1.5
	10	10.7	|	|	|
	20	10.7	|	|	|
50	0	14	8	|	|
	10	12.3	|	|	|
	20	12.3	|	|	|

a Fourier law with $\kappa = 1.5\,\mathrm{W\ m^{-1}K^{-1}}$, which is consistent with the value reported for a-Si using the same inter-atomic potential [46].

The parameters used to obtain the profiles in the crystalline part are reported in Table 2. The easiest parameter to interpret is C, which modifies the flux at the limit of the crystalline core. It depends on the specularity of phonon scattering at the boundary [42]. It appears clearly in Fig. 4 that the flux within the last 2.5 Å crystalline layer before the boundary is more or less the same whether there is an amorphous shell or not. This justifies why the value of C with or without the amorphous shell is the same. On the other hand, the non-local length ℓ characterizes the distance over which the flux is affected by the boundary, and it can be understood as a length over which the flux is self correlated. If assuming the multiscale relaxation time approximation (RTA) to simplify the collision operator, the non-local length can be expressed in terms of the phonon velocities and relaxation times as follows [9]:

$$\ell^2 = \frac{1}{5}\frac{\langle v_{g,\mathbf{q}}^3/v_{p,\mathbf{q}}\tau_{\mathbf{q}}^2\rangle}{\langle v_{g,\mathbf{q}}/v_{p,\mathbf{q}}\rangle}. \tag{7}$$

with $v_{g,\mathbf{q}}$ the group velocity, $v_{p,\mathbf{q}}$ the phase velocity, and $\tau_{\mathbf{q}}$ the relaxation time of the mode $\mathbf{q}$ and the bracket denoting an average weighted by the contribution of each mode $\mathbf{q}$ to the thermal capacity C_v, $\langle x_{\mathbf{q}}\rangle = \int \hbar\omega_{\mathbf{q}} x_{\mathbf{q}} \partial_T f_{\mathbf{q}}^{eq} d\mathbf{q}/C_v$.

In the present situation, ℓ characterizes how deeply in the core the flux is impacted by the free surface or interface. Again, in Fig. 4 the flux starts high in the center and is more or less constant until R = 20 Å, for both cases. Thus, neither ℓ nor C can explain the heat flux profile modifications appearing with the addition of an amorphous shell. Therefore, the influence of the amorphous shell cannot be directly related with a significant modification of boundary scattering within this model. The decrease of the saturation value is best modeled as a decrease of the effective intrinsic thermal conductivity κ_{Hyd} in Eq. (1). By using the RTA within the model described by Sendra et. al [9], the thermal con-

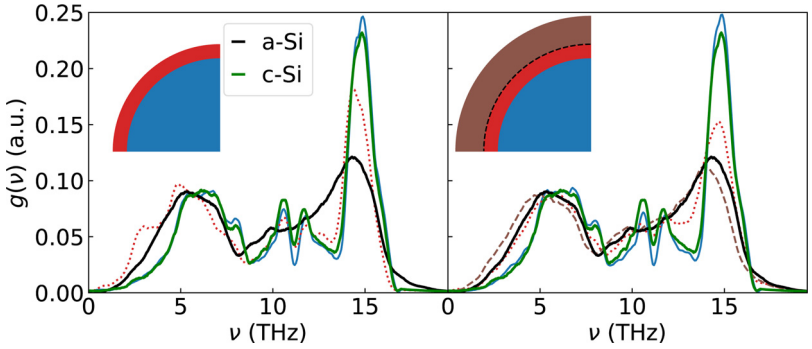


Fig. 5. Partial VDOS of the different layers in the nanowires of R_{Cry}= 37.5 Å and e = 0 (left panel) or 10 Å (right panel), the VDOS of bulk a-Si and c-Si are also depicted in, respectively, black and green full lines. The insets give the different colors associated with the different layers of the NW. In the inset, the black dashed line represents the crystalline/amorphous interface. (For interpretation of the references to colour in this figure legend, the reader is referred to the web version of this article.)

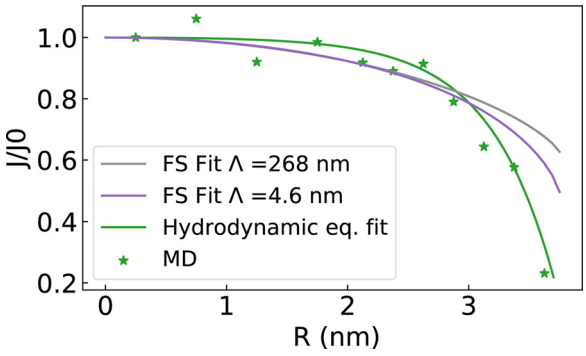


Fig. 6. Radial flux distribution for R_{Cry}=37.5 Å without shell, the results from NEMD are displayed as stars, the green line gives the hydrodynamic equations fit, the grey line the fit using the Fuchs-Sondheimer model with the MFP of bulk Si, and the purple line the Fuchs-Sondheimer model using a value of Λ least-square fitted to reproduce NEMD results. (For interpretation of the references to colour in this figure legend, the reader is referred to the web version of this article.)

ductivity can be expressed as follows:

$$\kappa_{Hyd} = \frac{1}{3} C_v \langle v_{g,\mathbf{q}}^2 \tau_{\mathbf{q}} \rangle, \tag{8}$$

with the same notation as in Eq. (7).

According to expression (8), the variation of κ_{Hyd} might be explained by variations of the group velocity or of the lifetime. However, addition of the amorphous shell does not impact the phonon dispersion in the direction of the propagation (see Appendix C), and thus does not impact the group velocity v_g. An impact over the relaxation times is thus the only remaining explanation of the decrease in thermal conductivity, but the lifetimes also affects the non-local length, that is constant. However, the lifetimes (or mean free paths $\Lambda_{\mathbf{q}} = \tau_{\mathbf{q}} v_{g,\mathbf{q}}$) are more influenced by the shell for high frequency modes (see Appendix C). As ℓ is less sensitive to the variation of the relaxation time at high frequencies than κ_{Hyd}, it may explain why κ_{Hyd} is impacted by the shell whereas ℓ remains unaffected.

For comparisons sake, the results obtained with MD have also been fitted using an analytical solution of the radial flux distribution in a cylindrical NW derived from the BTE, known as the Fuchs-Sondheimer model. This model has been used in multiple similar study [29]. The analytical solution for a cylinder is given by Dingle and Bragg [47] and reads:

$$\frac{j(r)}{j_0} = 1 - \frac{6}{\pi}(1-p)\sum_{\nu=0}^{\infty} p^{\nu} \int_0^{\pi/2} \cos^2\theta \sin\theta \times \int_0^{\pi/2} \cosh\left(\frac{r\sin\phi}{\Lambda\sin\theta}\right) \exp\left[-\frac{(2\nu+1)\sqrt{R^2 - r^2\cos^2\phi}}{\Lambda\sin\theta}\right] d\phi d\theta \tag{9}$$

with R the total radius, p the specularity parameter and Λ the MFP. The results obtained with this model in our case are displayed in the Fig. 6 in grey and purple and compared to the results obtained with MD. To model the flux with Eq. (9) we used $p = 0$ and two values for Λ. The first value is the average one of c-Si at 300 K, 268 nm [29] and results in the grey curve, the second one is obtained using a least square algorithm to fit the value of Λ to reproduce the NEMD results and results in the purple curve. Finally, we note that increasing the specularity p in expression (9) further decreases the quality of the fits. It appears clearly that neither values of the MFP can reproduce the results obtained by NEMD, in agreement with previous observations for similar NWs [29]. The fit using Eq. (1) gives more satisfying results, in particular near the interface.

From these observations, one may conclude that an approach that only considers the boundary scattering and a global mean free path cannot reproduce the results obtained with NEMD as well as the hydrodynamic model does.

In summary, it is shown that the heat flux radial distribution in a crystalline NW is comparable to a Poiseuille flow. Its maximum is in the center of the NW and decreases as it comes closer to the free surface or interface. The flux at the crystalline boundary is similar whether there is an amorphous shell or not. The main effect of the shell is to reduce the saturation flux value in the center of the NW. Such a flux profile can be reproduced with the hydrodynamic heat transport Eqs. (1), (3) and (4), with the effect of shell on the flux in the core reproduced by a decrease of the thermal conductivity parameter κ_{Hyd} in the crystalline core. In the amorphous shell, the flux does not depend on the radius and can be modeled by Fourier's law. Before pushing the analysis further, it is interesting to study the effect of the variation of the shell thickness and crystalline core radius.

3.3. impact of diameter and shell thickness on radial distribution of heat flux

In this section, size effects are explored with a study of the impact of the R_{Cry} and e. To this end, both R_{Cry} values and the two shell thicknesses are considered. The flux for the different R_{Cry} are represented in Fig. 7, without shell (left panel) or with a 10 or 20 Å shell (right panel). As in Fig. 4 the dots report the values in the different layers obtained through NEMD simulations, and the full lines the distribution modeled by the hydrodynamic heat transport Eqs. (1), (3) and (4). The vertical black full and dashed line represent, respectively, surface/interface position for R_{Cry}=37.5 and 50 Å. The profiles are very similar for the two crystalline radii. The main difference is the saturation level that increases upon increasing the crystalline radius. As observed in Fig. 4, the flux decreases near the core/shell interface and has the same value in the amorphous shell for the two radii.

The flux distributions for shells of 10 and 20 Å are displayed in the right panel of Fig. 7. The reported values are very similar for both shell thicknesses. This shows that the shell thickness does not affect the flux in the crystalline core. The MD simulated flux values for radial positions below 15 Å in the case of the small NW and the thicker shell (R_{Cry} = 37.5 Å and e = 20 Å in gray) do not fit this analysis. However, as in the first homoaxial cylinders, the average in Eq. (5) is performed over less atoms and thus more statistical variations can be expected.

The parameters used to reproduce the distributions with the hydrodynamic heat transport equations are reported in Table 2. It first appears that the same value is used for the slip coefficient C in each case. This could be predicted from the similarity of the flux at the interface in the different cases. Then as the radius increases, κ_{Hyd} is increased to reach the higher saturation level in the center of the NW. Again, this value is slightly reduced upon the addition of a shell. The non-local length ℓ is also increased from 5 Å to 8 Å when switching from R_{Cry}=37.5 to 50 Å. A similar effect has already been found for telescopic NWs [30]. Again, it is worth noting that both κ_{Hyd} and ℓ in Eq. (5) are linked to the phonon lifetime, that increases as the radius increases, so this can explain the variations of κ_{Hyd} and ℓ (see appendix Appendix C).

In conclusion, the presence or absence of the shell modifies the radial heat flux profile and hence the fitted parameter κ_{Hyd} for the hydrodynamic model changes, but modifying the shell thickness has no impact on any parameter value. On the other hand, increasing the radius of the core causes both an increase of the flux in the center of the NW (increase of κ_{Hyd}), and modifies the curvature of the heat flux profile (increase of ℓ).

4. Discussion

The radial heat flux distribution in NWs have the shape of a Poiseuille flow of fluid in a pipe: the flux is maximum in the cen-

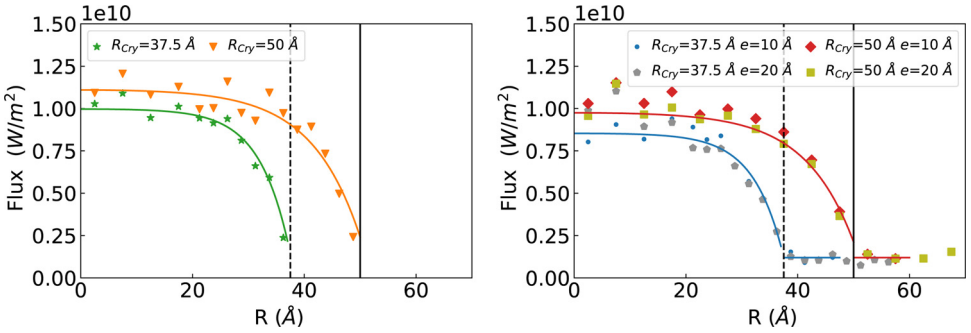


Fig. 7. Radial flux distribution for R_{Cry}=37.5 and 50 Å, without shell (left), and with a shell (right). The green, blue, and gray represent respectively the value without shell and with a 10 or 20 Å thick shell for R_{Cry}=37.5 Å. Likewise, the orange, red, and olive represent respectively the value without a shell and with a 10 or 20 Å thick shell for R_{Cry}=50 Å. The full lines represent the flux profile obtained from the hydrodynamic model fits. (For interpretation of the references to colour in this figure legend, the reader is referred to the web version of this article.)

ter and decreases toward the interface. For the first time we show that, this shape is not influenced by the addition of an amorphous shell, nevertheless the shell impacts the value of heat flux in the center of the NWs. The flux decrease appears at a distance of 20 Å from the free surface or crystalline/amorphous interface. This is similar to what was found through MD and Monte-Carlo simulations [29], and with MD and hydrodynamic heat transport equation without shell [30]. Furthermore, the wave-packet propagation hints to a similar heat flux profile.

This flux distribution can be modeled using the hydrodynamic heat Eq. (1) with fitted parameters. Within this model the only parameter that is affected by the addition of the amorphous shell is κ_{Hyd}, and not the parameters directly associated with boundary scattering (C and ℓ). Wingert et al. had already predicted that boundary scattering alone could not predict the low conductance of NWs, interestingly they have also shown that the group velocity could not explain this decrease of thermal conductivity [23]. The increase of R_{Cry} increases both ℓ and κ_{Hyd}. As the dispersion relations are not affected, neither by R_{Cry} nor by the shell presence or thickness (see Appendix C), the variations of those parameters are probably due to variation of the MFP/relaxation time, as discussed in 3.2.

However, a decrease in MFP is not the only hypothesis that could explain a decrease of κ_{Hyd}. By definition, the thermal conductivity in Eq. (1) considers that the behavior is ballistic at the microscale (it is based on the phonon gas picture). However, Fig. 2 shows that at high frequency, part of the transport is diffusive in the core and in the shell. A partially diffusive transport usually corresponds to an amorphous like thermal conductivity, for which the phonon gas model breaks down [48,49]. This transition contributes to a decrease of κ_{Hyd}, since the diffusive part becomes more important at the expense of the dominant ballistic part, and manifests itself as decay of the κ_{Hyd} in Eq. (1).

The lack of impact of the shell thickness on the heat flux radial distribution shape apparently contradicts the results of Shao et al. [50] who reported that the specularity is decreased when the thickness of the shell increases. However, in their definition of specularity they included the diffusion in the amorphous shell, whereas here only the reflections at the crystalline/amorphous interface are considered. This also contradicts the interpretation of the decrease in thermal conductivity in the core-shell NW as an effect of a reduction of the specularity in phonon-boundary collisions due to the presence of the amorphous layer [24]. Indeed, the specularity coefficient in the slip boundary condition (4) characterized from the MD profiles does not depend on the presence of the shell. Therefore, we conclude that the reduction of the global thermal conductivity due to the addition of the shell cannot be explained by reduction of the specularity at the boundary of the crystalline core. Consistently, we did not observe any substantial recrystallisation of the shell nor amorphisation of the crystal that would make the crystalline/amorphous interface rougher than the free surface. Also, previous studies have defined the surface to volume ratio as a universal gauge to study the thermal conductivity of NWs, however here the variation between the NWs diameters is too small to use this scale [51]. Moreover, coherent effects have been described in core-shell NWs [28], however, here, as the radial distribution does not depend on the amorphous shell thickness, it is unlikely that its variation upon addition of a shell is solely caused by resonance effects between the core and shell.

To conclude the comparisons with other modeling approaches, we note that the Fuchs-Sondheimer model, which uses a kinetic interpretation of the boundary effects [47], cannot reproduce the results obtained with MD (see Fig. 6). This suggests that alternative approaches describing the collective behavior of the heat carriers, like the non-local effects included in Eq. (1), are needed.

The radial energy distribution of the wave-packet in A.1 can be compared with the NEMD results in Figs. 4 and 7. For instance, little energy is transported ballistically in the amorphous shell. This is consistent with diffusive transport in amorphous Si [17]. This diffusive transport explains that the heat flux transport in the amorphous shell can be approximated by Fourier's law. Here, we show that the presence of the amorphous shell induces a diffusive transport in the crystalline core as well. Secondly, going closer to the interface/surface, there is less energy transmitted. For most of the explored frequencies, the highest energy concentration is reached in the center of the NW. This energy distribution can be seen as a qualitative measure of the flux at different frequencies. The reported energy density, multiplied by the group velocity, would give an approximate flux at each frequency. However, this approach is too crude for a direct heat flux estimation, as the frequencies need to be weighted according to the Bose Einstein distribution and the propagation direction/polarization considered, as done in previous works [17]. Nevertheless, the radial distribution of energy in the WPs indicates that the individual heat carriers may already favor a Poiseuille-like radial distribution of the heat flux.

The simulations carried out cannot be compared to the continuous hydrodynamic model within the limit of its validity. As stated in Section 2.2, in the original implementation of hydrodynamic heat transport equations, ℓ and κ_{Hyd} are estimated from *ab initio* simulations on the bulk properties of silicon [9]. This estimation gives a value of a few hundred of nanometers for ℓ. However, in the present case, the diameter of the NW (7.5 nm) is below half this value, so that the *ab initio* computed parameters are no longer valid [42]. They are replaced by empirical values, to fit the results

obtained with the NEMD method. The resulting curves correspond well to the NEMD results, not only in the present study, but also in a previous work [30]. Even though the *ab initio* calculated parameters cannot be used, it is shown here that the phenomena observed in the NEMD simulations can be captured with Eq. (1).

Additionaly, the determination of thermal conductivity with NEMD shows strong size effects [16] so that the radial distribution obtained may depend on the length of the NW. This effect could even impact more the NWs without shell [34]. Even though the point of this study is to compare the distribution of heat flux with or without an amorphous shell at constant length, an impact of the length is expected since even in NWs of the diameter considered here, phonons with a large MFP are expected to play an important role on thermal conductivity [52]. This importance of long MFP phonons could induce size effects along the NW longitudinal direction.

Finally, we note that having an experimental validation of the observations is challenging. However, local measurement of conductance using SThM [53] could be used to study the local variation of the conduction on the cross-section of a cut NW.

5. conclusion

The radial heat flux distributions in nanowires of diameter 7.5 or 10 nm, pure pristine or with an amorphous shell, have been studied with three methods: wave-packet propagation, NEMD and the hydrodynamic heat equation. For all NWs, the radial heat flux profile in the crystalline part is similar: it looks like a Poiseuille fluid flow. The addition of an amorphous shell decreases the heat flux in the center of the NW, but the flow at the boundary of the crystalline part is not affected by the presence of a shell. To go further, this profile can be reproduced with the Eqs. (1), (3) and (4), using empirical values for the equation parameters. Doing so, it appears that the addition of the shell can be reproduced by a decrease in the thermal conductivity used to model the transport in the crystalline core. The non-Fourier parameters of the equation do not appear to be impacted by the shell for the geometries considered, and can thus be understood as intrinsic parameters of the crystalline core. As a result, within this model, the effect of the shell is global, rather than localized at the interface. Accordingly, the amorphous shell does not impact the specularity of the phonon-boundary collisions. The effective thermal conductivity decrease may be linked to a partially diffusive heat transport, together with a modification of the MFP spectra, which motivates frequency dependent analysis of the thermal conductivity [54].

Declaration of Competing Interest

The authors declare that they have no known competing financial interests or personal relationships that could have appeared to influence the work reported in this paper.

CRediT authorship contribution statement

Paul Desmarchelier: Methodology, Software, Formal analysis, Writing – original draft, Visualization. **Albert Beardo:** Methodology, Software, Writing – original draft, Writing – review & editing. **F. Xavier Alvarez:** Funding acquisition, Supervision, Resources, Writing – review & editing, Conceptualization. **Anne Tanguy:** Funding acquisition, Methodology, Supervision, Resources, Writing – review & editing, Conceptualization. **Konstantinos Termentzidis:** Funding acquisition, Supervision, Resources, Writing – review & editing, Conceptualization, Project administration.

Acknowledgment

This work was granted access to the HPC resources of IDRIS under the allocation 2021-A0110911092, made by GENCI. A.B. and F.X.A acknowledge financial support by the Spanish Ministerio de Ciencia, Innovación y Universidades under Grant No. RTI2018-097876-B-C22 (MCIU/AEI/FEDER). This work was made possible thanks to a Ph.D. scholarship accorded by the French Ministry of Education and Higher Education. We want to thank J. Camacho for fruitful discussions.

Appendix A. Methods

A1. wave-packet propagation

The radial distribution of energy propagation in the NWs can also be studied through the propagation of wave-packets. This can help the representation of the flux and to get more physical insights of what is happening at the interfaces. They can, for example, inform on the shape and pathways taken by individual phonons in the nanostructures [46]. The method used here is very similar to the method used for asymmetric core-shell NWs [37]. An impulsion at a given frequency is imposed on a 2 Å slice in the middle of the NW, and the resulting energy propagation is monitored. The WP is generated through a Gaussian windowed sinusoidal force excitation,

$$f = A\sin[2\pi\nu(t-3\tau)]\exp\left[-\frac{(t-3\tau)^2}{(2\tau^2)}\right], \tag{A.1}$$

that is imposed to the atoms in the central slice. The amplitude A is 3.773×10^{-4} eV Å^{-1-1}. The spreading of the Gaussian window τ is selected to be sufficiently small to offer a compromise between spatial extension of the WP compared to the system length and the resolution in the frequency space. The used value is 0.36 ps.

In these simulations, the impulsion is the only source of movement, the initial velocities are set to 0, and the system is at mechanical equilibrium. The simulations are done at constant energy (once the excitation is done), with a time step of 1×10^{-3} ps. Periodic boundary conditions are used in the direction of propagation.

A2. thermal conductivity via non equilibrium molecular dynamics

To estimate the radial flux distribution in core-shell NWs, the first step is to create a thermal gradient across them. This is done by using a hot thermostat on one side of the NW and a cold one on the other side (as depicted in Fig. A.8 a). This set up corresponds to the usual NEMD set up [55].

Before establishing the thermal gradient, the NWs are first equilibrated at 300 K in two steps, a first step with a Nosé-Hoover thermostat and a Nosé-Hoover barostat allowing the thermal expansion in the growing direction of the NWs for 5 ps. In a second step, the boundary conditions are switched from periodic to fixed in the growing direction, and the atoms within 10 Å of the extremities are fixed to avoid free surface effects. Once the boundary conditions are set, the atoms between the two fixed regions are equilibrated at 300 K for 50 ps with a Nosé-Hoover thermostat. Only after this step, the atoms from 10 to 20 Å from the extremities are thermostated at 320 K on one side and at 280 K on the other. In these thermostats, a simple velocity rescaling is used. The trajectories of the atoms are computed using the usual velocity Verlet integration scheme, implemented in LAMMPS [56]. The flux is averaged from 1000 ps to 2000 ps, when the steady state is reached. This steady state is defined here by the stabilization of the temperature profile through the whole NW, and the fact that the energy exchanged by the thermostats and the NW increases linearly with time. For better statistics, these simulations are repeated 5 times

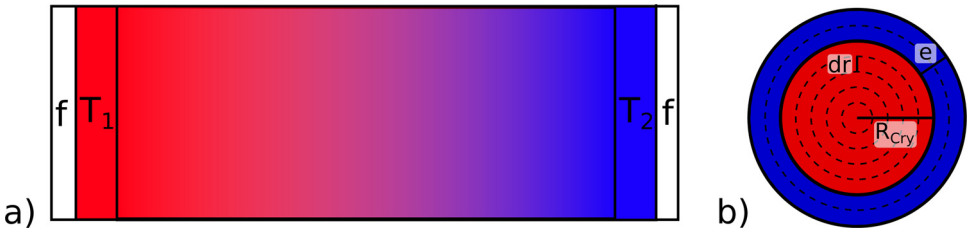


Fig. A1. a) Position of the fixed atoms (f) and hot (T_1) and cold (T_2) thermostat for the NEMD simulation, b) schematic representation of the cross-section with R_{Cry} the radius of the crystalline core (in red) and e the thickness of the amorphous layer (in blue). The dotted lines represent the discretization of the radius for the computation of the flux as a function of the radius. (For interpretation of the references to colour in this figure legend, the reader is referred to the web version of this article.)

Table A1
Global thermal conductivity obtained for the nanowires through the NEMD method using Eq. 5.

R_{Cry} (Å)	e (Å)	κ_{MD} ($Wm^{-1}K^{-1}$)
37.5	0	8.9
	10	5.7
	20	4.3
50	0	9.9
	10	6.9
	20	5.3

for each configuration, with each time a different initial velocity distribution. The time step used is of 5×10^{-4} ps.

During those simulations, the flux is computed in homoaxial hollow cylinders of thickness $dr = 2.5$ or 5 Å (see Fig. A.8b). The heat flux in each shell is computed using every atom in the shell from 10Å away from the cold thermostat to 10 Å away from the hot thermostat. Each studied configuration is listed in Table 1. For R_{Cry}= 50 Å with e= 10 Å and 20 Å the dr is larger to decrease computing time. The flux is computed with the Eq. (5), sampled every 0.5 ps, and averaged over the steady state. Eq. (5) involves a sum over the atoms normalized by a volume, so that in the center of the NW there are fewer atoms per shell. This decreased number of atoms increases the variability of the computed flux, in particular, for $dr = 2.5$ Å. For this reason, the average over two homoaxial hollow cylinders is used for radii smaller than 20 Å.

In Table A.3, the thermal conductivity κ_{MD} extracted from the NEMD simulation is also displayed, in line with what is expected: κ_{MD} decreases with the amorphous shell thickness (e) and increases with R_{Cry}, as reported in previous studies [35,39].

A3. vibrational density of states

The vibrational density of states (VDOS) are evaluated through the Fourier transform of the velocity auto-correlation function (VACF) [6]. To this end, the system is first equilibrated at 50 K for 100 ps with a Nosé-Hoover thermostat. After this, the thermostats are switched off, and the system evolves at constant energy. Over this 100 ps long simulation, the VACF averaged over the particles belonging to the different concentric homoaxial hollow cylinders of the NWs (see Fig. A.8b) is computed and recorded. To get the (partial) VDOS, the Fourier transform of the VACF for the different homoaxial cylinders are finally computed and filtered using a polynomial filter.

A4. phonon dispersion via the dynamical structure factor

The dynamical structure factor (DSF) is a spatial and temporal Fourier transform of the atomic displacements used to characterize the vibrational properties of a system. It is computed with the same method as in a previous publication [46]. First, the sample is heated to 300 K and equilibrated at this temperature for 50 ps using a Nosé-Hoover thermostat. After this, the atomic trajectories are recorded during a 10 ps long constant energy simulation, the position being recorded every 1×10^{-2} ps. Then, the DSF is computed using the following expression:

$$S(\mathbf{q},\omega) = \frac{2}{NT}\left|\sum_{i}^{N_{at}} \exp(-i\mathbf{q}\cdot\mathbf{r_i}) \int_0^{\tau} \mathbf{u_i}(r_i,t)\cdot\mathbf{m}_\eta exp(i\omega t)dt\right|^2, \tag{A.2}$$

with $\mathbf{q}$ the wave-vector, $\mathbf{u_i}$ and $\mathbf{r_i}$ the displacement and position of the i^{th} atom, $\boldsymbol{m}_\eta$ the polarization vector (parallel or perpendicular to $\mathbf{q}$), T the temperature and N the total number of atoms [49]. The DSF can be obtained for the different vectors of the Brillouin zone. In this study, the focus is laid on the propagation in the axial direction of the NW, that is in the ⟨100⟩ lattice direction, corresponding to ΓX in the reciprocal space. From the DSF, the phononic dispersion curves can be obtained. For this, the DSF is first filtered through a convolution with a typical energy resolution curve of line-width 0.33 THz (as suggested by Tlili et al. [17]). Then, for a given wave-vector direction, the dispersion is estimated from the frequency for which the DSF has the highest value for each wave vector within the frequency range of acoustic phonons. Once each wave vector has a value, the curve is filtered using a Savitzky-Golay polynomial filter. The DSF can also be fitted with a damped harmonic oscillator model (DHO) [49],

$$S_\eta(q,\nu) = \frac{A}{4\pi^2\left((\nu^2-\nu_\eta^2(q))^2+\omega^2\Gamma^2\right)} \tag{A.3}$$

with $\Gamma = 1/\tau$ the inverse lifetime, $\nu(q)$ the phonon dispersion and A the amplitude. This allows the estimation of the lifetime/mean free path.

Appendix B. Frequency Dependence of Radial Energy Distribution

An overview of the behavior at the different frequencies is given in Fig. B.9. In this figure, the energy distribution profile is given for the timestep for which the highest energy in any homoaxial hollow cylinder is reached. This corresponds to the curve of Fig. 3 at the time step where the highest value is reached locally, for each frequency.

All the frequencies share a common tendency: there is little energy transmitted near the free surface/interface. The only exceptions are at 14 THz where the maximum is near the interface and at 2 THz with the wave at the surface. Moreover, the maximal amplitude is not always in the center of the NW: for 8 and 10 THz without shell and for 8 THz with a shell, the maximum is around R=20 Å. It is worth noting that the amount of energy injected in the system depends on the frequency used, so that the quantity of energy at the different frequencies are not directly comparable.

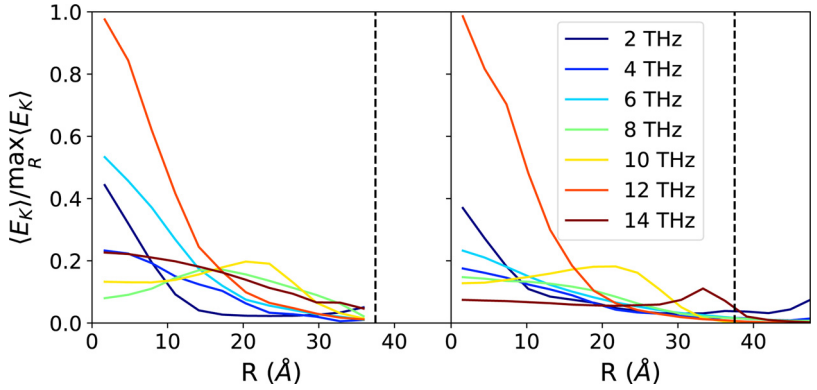


Fig. B1. Atomic kinetic energy as a function of the radius averaged on a portion of the NWs 90 to 160 Å away from the excited layer, for the time step where the maximal intensity is reached. For the nanowires of R_{Cry}= 37.5 Å and e = 0 (left panel) or 10 Å (right panel). The vertical black dashed line represents the end of the crystalline core.

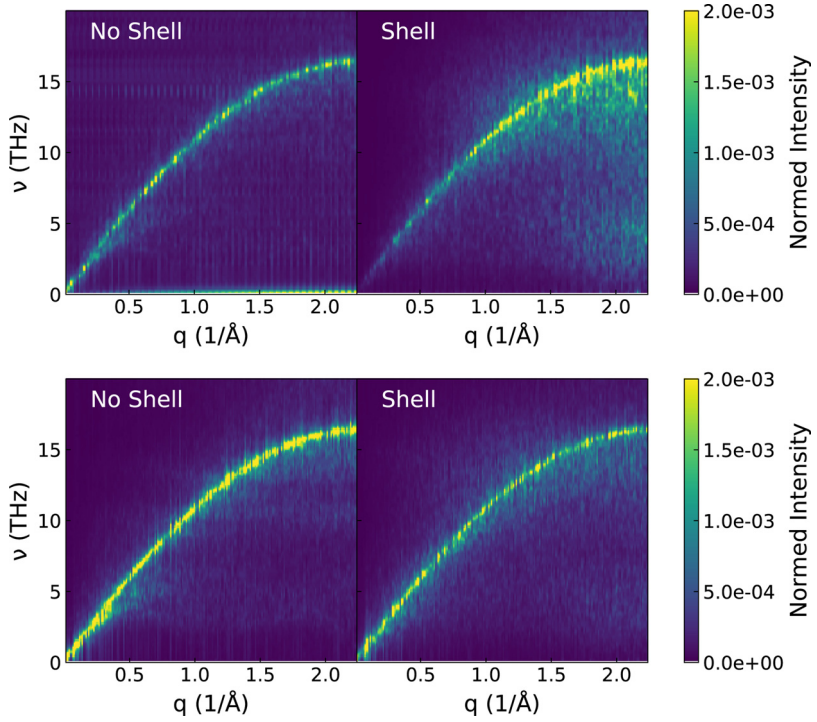


Fig. C1. Dynamical structure factor in the ΓX direction, projected on the longitudinal polarization for the nanowires of R_{Cry}= 37.5 Å (top) and of R_{Cry}= 50 Å (bottom), without (left) or with an amorphous shell of thickness e=10 Å (right).

Appendix C. Dynamical Structure Factor and Mean Free Path

The influence of the shell on the parameters of the hydrodynamic heat transport equation could be explained by a modification of the dispersion relation. Indeed, both κ and ℓ depend on the group velocity (that is, the derivative of the dispersion relation) and the relaxation time (see Eqs. (7) and (8)). The DSF for the different configurations are displayed in Fig. C.10. Even before the extraction of the dispersion relations, it appears that the main features of the DSF, with or without amorphous shell, are very similar. In both cases, the acoustic branch appears clearly between 0 and 17 THz. The main difference between the two is the background noise, appearing in the DSF when there is an amorphous shell. This corresponds to a-Si modes. It is also to be noted that a small branch at low frequencies associated to surface modes appears [57]. This is consistent with the observation of the wave at the surface in Fig. 2. For the larger diameter (bottom panel), the same observation can be made, though the background noise is less marked.

The dispersion relations extracted from the DSF, are displayed in Fig. C.11. It appears clearly that the different curves superimpose nicely. So that neither the shell nor the radius impact the dispersion relation in the NW for the propagation in the principal direction, and thus does not impact the group velocity either.

The remaining microscopic quantity that can be linked to the mesoscopic transport parameters is the MFP. It can be extracted from the DSF (see section A.4) and is given by the enlargment of the DSF around the line of maximum intensity. The results are displayed in Fig. C.11. The MFP of high frequencies phonons, above 6 THz, is smaller in the presence of an amorphous shell. This variation can be linked to the linewidth increase (and thus MFP decrease) due to the amorphous modes visible in Fig. C.10 for the NW with an amorphous shell. The decrease of the MFP at high frequencies induced by the shell appears clearly for the two radii. However, as the MFP with a shell for the two radii are very close, it is not possible to conclude that the increase in thermal conductivity linked to a variation of the MFP in this direction. The MFPs obtained with this method are notably small compared to the re-

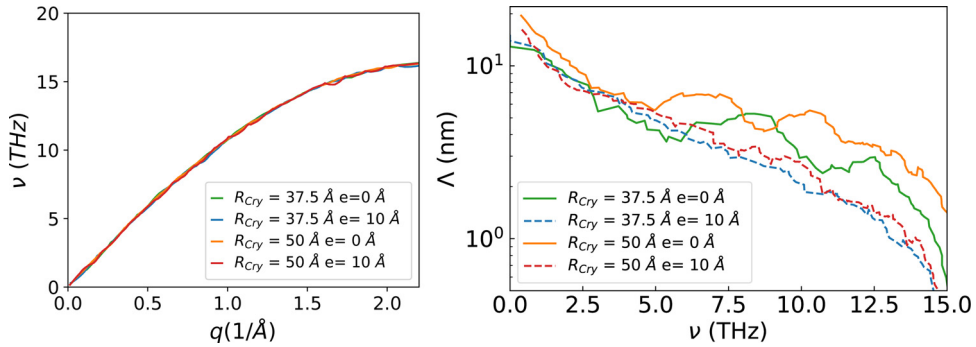


Fig. C2. Dispersion relations extracted from the DSF (right), MFP as extracted using the DHO from the DSF for the nanowires of R_{Cry}= 37.5-50 Å and $e = 0$ (green-orange) or 10 Å (blue-red). (For interpretation of the references to colour in this figure legend, the reader is referred to the web version of this article.)

sults obtained for similar NWs using the time domain normal-mode analysis [58] but of the order of the results obtained with wave-packet propagation [37]. However, the large increase in MFP at high frequencies observed with wave-packet propagation is notably absent when computed with this method.

This MFP decrease, due to the addition of the amorphous shell, could partially explain the decrease in thermal conductivity. Even if the relaxation time appears in both expressions of ℓ and κ, it is not weighted equivalently in both expressions. Consequently, the MFP variations within a certain range of frequencies may affect the two parameters differently.

As ℓ is less sensitive to the variation of the relaxation time at high frequencies than κ, the variation of the MFP as a function of frequency may explain why κ is affected by the shell whereas ℓ is unaffected. However, as the MFP is measured on the whole NW including the amorphous shell the decrease obtained in Fig. C.11 might be overestimated. Finally, part of the energy could also be supported by diffusive (non-ballistic) phonons.

References

[1] R. Peierls, Zur kinetischen theorie der wärmeleitung in kristallen, Ann. Phys. 395 (8) (1929) 1055–1101. https://onlinelibrary.wiley.com/doi/epdf/10.1002/andp.19293950803

[2] P.G. Klemens, F.E. Simon, The thermal conductivity of dielectric solids at low temperatures (theoretical), Proc. R. Soc. Lond. Ser. A. Math. Phys. Sci. 208 (1092) (1951) 108–133, doi:10.1098/rspa.1951.0147.

[3] C. Cattaneo, Sulla conduzione del calore, Atti Sem. Mat. Fis. Univ. Modena 3 (1948) 83–101.

[4] J. Callaway, Model for lattice thermal conductivity at low temperatures, Phys. Rev. 113 (1959) 1046–1051, doi:10.1103/PhysRev.113.1046.

[5] D. Lacroix, K. Joulain, D. Lemonnier, Monte carlo transient phonon transport in silicon and germanium at nanoscales, Phys. Rev. B 72 (2005) 064305, doi:10.1103/PhysRevB.72.064305.

[6] M.T. Dove, M.T. Dove, C.U. Press, M.F. Hochella, R.C. Liebermann, A. Putnis, Introduction to lattice dynamics, Cambridge Topics in Mineral Physics and Chemistry, Cambridge University Press, 1993. https://books.google.fr/books?id=jpe2aYwF3v0C

[7] W. Zhang, T.S. Fisher, N. Mingo, The atomistic green's function method: an efficient simulation approach for nanoscale phonon transport, Numer. Heat Transfer, Part B 51 (4) (2007) 333–349, doi:10.1080/10407790601144755.

[8] P. Torres, A. Ziabari, A. Torelló, J. Bafaluy, J. Camacho, X. Cartoixà, A. Shakouri, F.X. Alvarez, Emergence of hydrodynamic heat transport in semiconductors at the nanoscale, Phys. Rev. Mater. 2 (2018) 076001, doi:10.1103/PhysRevMaterials.2.076001.

[9] L. Sendra, A. Beardo, P. Torres, J. Bafaluy, F.X. Alvarez, J. Camacho, Derivation of a hydrodynamic heat equation from the phonon boltzmann equation for general semiconductors, Phys. Rev. B 103 (2021) L140301, doi:10.1103/PhysRevB.103.L140301.

[10] R.A. Guyer, J.A. Krumhansl, Thermal conductivity, second sound, and phonon hydrodynamic phenomena in nonmetallic crystals, Phys. Rev. 148 (1966) 778–788, doi:10.1103/PhysRev.148.778.

[11] Y. Guo, D. Jou, M. Wang, Nonequilibrium thermodynamics of phonon hydrodynamic model for nanoscale heat transport, Phys. Rev. B 98 (2018) 104304, doi:10.1103/PhysRevB.98.104304.

[12] A. Beardo, J.L. Knobloch, L. Sendra, J. Bafaluy, T.D. Frazer, W. Chao, J.N. Hernandez-Charpak, H.C. Kapteyn, B. Abad, M.M. Murnane, F.X. Alvarez, J. Camacho, A general and predictive understanding of thermal transport from 1d- and 2d-confined nanostructures: theory and experiment, ACS Nano 15 (8) (2021) 13019–13030, doi:10.1021/acsnano.1c01946.

[13] A. Beardo, M.G. Hennessy, L. Sendra, J. Camacho, T.G. Myers, J. Bafaluy, F.X. Alvarez, Phonon hydrodynamics in frequency-domain thermoreflectance experiments, Phys. Rev. B 101 (2020) 075303, doi:10.1103/PhysRevB.101.075303.

[14] R.J. Hardy, Energy-flux operator for a lattice, Phys. Rev. 132 (1963) 168–177, doi:10.1103/PhysRev.132.168.

[15] R. Kubo, Statistical-mechanical theory of irreversible processes. i. general theory and simple applications to magnetic and conduction problems, J. Phys. Soc. Jpn. 12 (6) (1957) 570–586.

[16] P.K. Schelling, S.R. Phillpot, P. Keblinski, Comparison of atomic-level simulation methods for computing thermal conductivity, Phys. Rev. B 65 (2002) 144306, doi:10.1103/PhysRevB.65.144306.

[17] A. Tlili, V.M. Giordano, Y.M. Beltukov, P. Desmarchelier, S. Merabia, A. Tanguy, Enhancement and anticipation of the iofferegel crossover in amorphous/nanocrystalline composites, Nanoscale 11 (2019) 21502–21512, doi:10.1039/C9NR03952J.

[18] P.C. Howell, Comparison of molecular dynamics methods and interatomic potentials for calculating the thermal conductivity of silicon, J. Chem. Phys. 137 (22) (2012) 224111, doi:10.1063/1.4767516.

[19] Q. Zheng, M. Hao, R. Miao, J. Schaadt, C. Dames, Advances in thermal conductivity for energy applications: a review, Progr. Energy 3 (1) (2021) 012002, doi:10.1088/2516-1083/abd082.

[20] R. Ghosh, P.K. Giri, Silicon nanowire heterostructures for advanced energy and environmental applications: a review, Nanotechnology 28 (1) (2016) 012001, doi:10.1088/0957-4484/28/1/012001.

[21] D. Li, Y. Wu, P. Kim, L. Shi, P. Yang, A. Majumdar, Thermal conductivity of individual silicon nanowires, Appl. Phys. Lett. 83 (14) (2003) 2934–2936, doi:10.1063/1.1616981.

[22] N.R. Shyamprasad, R. Rhyner, K. Vuttivorakulchai, M. Luisier, D. Poulikakos, Length scale of diffusive phonon transport in suspended thin silicon nanowires, Nano Lett. 17 (1) (2017) 276–283, doi:10.1021/acs.nanolett.6b04050. PMID: 28005386

[23] M.C. Wingert, Z.C.Y. Chen, E. Dechaumphai, J. Moon, J.-H. Kim, J. Xiang, R. Chen, Thermal conductivity of ge and gesi coreshell nanowires in the phonon confinement regime, Nano Lett. 11 (12) (2011) 5507–5513, doi:10.1021/nl203356h. PMID: 22112167

[24] A. Malhotra, M. Maldovan, Phononic pathways towards rational design of nanowire heat conduction, Nanotechnology 30 (37) (2019) 372002, doi:10.1088/1361-6528/ab261d.

[25] J. Lim, K. Hippalgaonkar, S.C. Andrews, A. Majumdar, P. Yang, Quantifying surface roughness effects on phonon transport in silicon nanowires, Nano Lett. 12 (5) (2012) 2475–2482, doi:10.1021/nl3005868. PMID: 22524211

[26] A.I. Hochbaum, R. Chen, R.D. Delgado, W. Liang, E.C. Garnett, M. Najarian, A. Majumdar, P. Yang, Enhanced thermoelectric performance of rough silicon nanowires, Nature 451 (7175) (2008) 163–167.

[27] F. Sansoz, Surface faceting dependence of thermal transport in silicon nanowires, Nano Lett. 11 (12) (2011) 5378–5382, doi:10.1021/nl2029688. PMID: 22050128

[28] G. Xie, D. Ding, G. Zhang, Phonon coherence and its effect on thermal conductivity of nanostructures, Adv. Phys. 3 (1) (2018) 1480417, doi:10.1080/23746149.2018.1480417.

[29] M. Verdier, Y. Han, D. Lacroix, P.-O. Chapuis, K. Termentzidis, Radial dependence of thermal transport in silicon nanowires, J. Phys. 2 (1) (2018) 015002, doi:10.1088/2515-7639/aaead5.

[30] C. Melis, R. Rurali, X. Cartoixà, F.X. Alvarez, Indications of phonon hydrodynamics in telescopic silicon nanowires, Phys. Rev. Appl. 11 (2019) 054059, doi:10.1103/PhysRevApplied.11.054059.

[31] Y. Cui, L.J. Lauhon, M.S. Gudiksen, J. Wang, C.M. Lieber, Diameter-controlled synthesis of single-crystal silicon nanowires, Appl. Phys. Lett. 78 (15) (2001) 2214–2216, doi:10.1063/1.1363692.

[32] L. Yang, B. Latour, A.J. Minnich, Phonon transmission at crystalline-amorphous interfaces studied using mode-resolved atomistic green's functions, Phys. Rev. B 97 (2018) 205306, doi:10.1103/PhysRevB.97.205306.

[33] A. France-Lanord, S. Merabia, T. Albaret, D. Lacroix, K. Termentzidis, Thermal properties of amorphous/crystalline silicon superlattices, J. Phys. 26 (35) (2014) 355801, doi:10.1088/0953-8984/26/35/355801.
[34] Y. Gao, W. Bao, Q. Meng, Y. Jing, X. Song, The thermal transport properties of single-crystalline nanowires covered with amorphous shell: a molecular dynamics study, J. Non Cryst. Solids 387 (2014) 132–138, doi:10.1016/j.jnoncrysol.2014.01.004.
[35] E. Blandre, L. Chaput, S. Merabia, D. Lacroix, K. Termentzidis, Modeling the reduction of thermal conductivity in core/shell and diameter-modulated silicon nanowires, Phys. Rev. B 91 (2015) 115404, doi:10.1103/PhysRevB.91.115404.
[36] X. Liu, G. Zhang, Q.-X. Pei, Y.-W. Zhang, Surface morphology and strain coupling effects on phonon transport in silicon nanowires, Mater. Today:. Proc. 3 (8) (2016) 2759–2765, doi:10.1016/j.matpr.2016.06.024. 6th International conference on Advanced Nano Materials
[37] P. Desmarchelier, A. Tanguy, K. Termentzidis, Thermal rectification in asymmetric two-phase nanowires, Phys. Rev. B 103 (2021) 014202, doi:10.1103/PhysRevB.103.014202.
[38] I. Bejenari, A. Burenkov, P. Pichler, I. Deretzis, A. La Magna, Molecular dynamics modeling of the radial heat transfer from silicon nanowires, in: 2020 International Conference on Simulation of Semiconductor Processes and Devices (SISPAD), 2020, pp. 67–70, doi:10.23919/SISPAD49475.2020.9241646.
[39] M. Verdier, D. Lacroix, K. Termentzidis, Roughness and amorphization impact on thermal conductivity of nanofilms and nanowires: making atomistic modeling more realistic, J. Appl. Phys. 126 (16) (2019) 164305, doi:10.1063/1.5108618.
[40] A. Beardo, M. López-Suárez, L.A. Pérez, L. Sendra, M.I. Alonso, C. Melis, J. Bafaluy, J. Camacho, L. Colombo, R. Rurali, F.X. Alvarez, J.S. Reparaz, Observation of second sound in a rapidly varying temperature field in ge, Sci. Adv. 7 (27) (2021), doi:10.1126/sciadv.abg4677.
[41] S. Lee, D. Broido, K. Esfarjani, G. Chen, Hydrodynamic phonon transport in suspended graphene, Nat. Commun. 6 (1) (2015) 1–10, doi:10.1038/ncomms7290.
[42] A. Beardo, M. Calvo-Schwarzwälder, J. Camacho, T.G. Myers, P. Torres, L. Sendra, F.X. Alvarez, J. Bafaluy, Hydrodynamic heat transport in compact and holey silicon thin films, Phys. Rev. Appl. 11 (2019) 034003, doi:10.1103/PhysRevApplied.11.034003.
[43] P. Boone, H. Babaei, C.E. Wilmer, Heat flux for many-body interactions: corrections to LAMMPS, J. Chem. Theory Comput. 15 (10) (2019) 5579–5587, doi:10.1021/acs.jctc.9b00252. PMID: 31369260
[44] Y. Zhou, Assessing the quantum effect in classical thermal conductivity of amorphous silicon, J. Appl. Phys. 129 (23) (2021) 235104, doi:10.1063/5.0054039.
[45] D. Donadio, G. Galli, Atomistic simulations of heat transport in silicon nanowires, Phys. Rev. Lett. 102 (2009) 195901, doi:10.1103/PhysRevLett.102.195901.
[46] P. Desmarchelier, A. Carré, K. Termentzidis, A. Tanguy, Ballistic heat transport in nanocomposite: the role of the shape and interconnection of nanoinclusions, Nanomaterials 11 (8) (2021), doi:10.3390/nano11081982.
[47] R.B. Dingle, W.L. Bragg, The electrical conductivity of thin wires, Proc. R. Soc. Lond. Ser. A. Math. Phys. Sci. 201 (1067) (1950) 545–560, doi:10.1098/rspa.1950.0077.
[48] P.B. Allen, J.L. Feldman, Thermal conductivity of disordered harmonic solids, Phys. Rev. B 48 (1993) 12581–12588, doi:10.1103/PhysRevB.48.12581.
[49] Y.M. Beltukov, D.A. Parshin, V.M. Giordano, A. Tanguy, Propagative and diffusive regimes of acoustic damping in bulk amorphous material, Phys. Rev. E 98 (2018) 023005, doi:10.1103/PhysRevE.98.023005.
[50] C. Shao, Q. Rong, N. Li, H. Bao, Understanding the mechanism of diffuse phonon scattering at disordered surfaces by atomistic wave-packet investigation, Phys. Rev. B 98 (2018) 155418, doi:10.1103/PhysRevB.98.155418.
[51] J. Chen, G. Zhang, B. Li, Phonon coherent resonance and its effect on thermal transport in core-shell nanowires, J. Chem. Phys. 135 (10) (2011) 104508, doi:10.1063/1.3637044.
[52] H. Zaoui, P.L. Palla, F. Cleri, E. Lampin, Length dependence of thermal conductivity by approach-to-equilibrium molecular dynamics, Phys. Rev. B 94 (2016) 054304, doi:10.1103/PhysRevB.94.054304.
[53] S. Gomès, A. Assy, P.-O. Chapuis, Scanning thermal microscopy: a review, Physica Status Solidi (a) 212 (3) (2015) 477–494, doi:10.1002/pssa.201400360.
[54] K. Sääskilahti, J. Oksanen, S. Volz, J. Tulkki, Frequency-dependent phonon mean free path in carbon nanotubes from nonequilibrium molecular dynamics, Phys. Rev. B 91 (2015) 115426, doi:10.1103/PhysRevB.91.115426.
[55] P.K. Schelling, S.R. Phillpot, P. Keblinski, Comparison of atomic-level simulation methods for computing thermal conductivity, Phys. Rev. B 65 (2002) 144306, doi:10.1103/PhysRevB.65.144306.
[56] S. Plimpton, Fast parallel algorithms for short-range molecular dynamics, J. Comput. Phys. 117 (1) (1995) 1–19, doi:10.1006/jcph.1995.1039.
[57] T. Zushi, K. Shimura, M. Tomita, K. Ohmori, K. Yamada, T. Watanabe, Phonon dispersion in ⟨100⟩ si nanowire covered with SiO2film calculated by molecular dynamics simulation, ECS J. Solid State Sci. Technol. 3 (5) (2014) P149–P154, doi:10.1149/2.010405jss.
[58] Y. Zhou, M. Hu, Record low thermal conductivity of polycrystalline si nanowire: breaking the casimir limit by severe suppression of propagons, Nano Lett. 16 (10) (2016) 6178–6187, doi:10.1021/acs.nanolett.6b02450. PMID: 27603153